Thermal and rheological behaviour of stearate-based phase change nanofluids

Prado, Jose I.; Navarro, María Elena; Calviño, Uxía; Ding, Yulong; Lugo, Luis

DOI:
10.1016/j.molliq.2023.122293

Document Version
Publisher's PDF, also known as Version of record

Citation for published version (Harvard):
Prado, JI, Navarro, ME, Calviño, U, Ding, Y & Lugo, L 2023, 'Thermal and rheological behaviour of stearate-based phase change nanofluids', *Journal of Molecular Liquids*, vol. 385, 122293.
https://doi.org/10.1016/j.molliq.2023.122293

Journal of Molecular Liquids 385 (2023) 122293

Contents lists available at ScienceDirect

Journal of Molecular Liquids

journal homepage: www.elsevier.com/locate/molliq

Thermal and rheological behaviour of stearate-based phase change nanofluids

Jose I. Prado [a,b,*], María Elena Navarro [a,*], Uxía Calviño [a,b], Yulong Ding [a], Luis Lugo [b]

[a] Birmingham Centre for Energy Storage, School of Chemical Engineering, University of Birmingham, B15 2TT Birmingham, United Kingdom
[b] CINBIO, Universidade de Vigo, Grupo GAME, Departamento de Física Aplicada, 36310 Vigo, Spain

ARTICLE INFO

Keywords:
Nanofluids
Phase change materials (PCM)
Magnesium oxide nanoparticles
Graphene nanoplatelets
Thermal diffusivity
Rheological behaviour

ABSTRACT

A comprehensive study has been performed on the thermal and rheological behaviour of two sets of isooctyl stearate (PureTemp 8, PT8) based nanofluids with different concentrations of spherical MgO nanoparticles (up to 15 wt%) and graphene nanoplatelets (up to 2 wt%). The results show that the presence of the nanomaterials does not significantly alter the phase change temperatures of the base fluids, although the latent heat decreases by 27% and 7.6% for 15 wt% MgO and 1.0 wt% GnP-based nanofluids, respectively. Both nanomaterials are found to increase the thermal diffusivity of the nanofluids. GnP-based suspensions have a higher thermal diffusivity than the MgO ones at similar nanomaterial concentrations. Rheological analyses show that MgO-PT8 nanofluids behave as a viscoplastic material (solid at zero shear rate); whereas the GnP-PT8 samples are viscoelastic (liquid at zero shear rate). MgO nanoparticles promote the formation of large fractal agglomerates, leading to a strong gel network of particles within PT8, while platelet-shaped GnP gives a fluid-like behaviour.

1. Introduction

Nanofluids have the potential to play an important role in sustainable energy systems and heat transfer applications [1]. Heat transfer enhancement has become of great interest in several fields over the last few decades, *e.g.* industrial applications [2], electronics [3], and energy technologies [4,5]. Traditionally, the enhancement of heat transfer has been done through extended surfaces (fins, microchannels), reaching almost its cost-effective limit [6]. The aim of adopting new strategies in heat transfer is to accommodate high heat fluxes and reduce capital costs. This would lead heat exchangers to work at smaller velocities and achieve the same or higher heat transfer coefficients while reducing the pressure drop of the HTF. In recent years, reports on the use of nanofluids as high-performance heat transfer fluids (HTFs) have been published [7] highlighting how they provide a higher heat transfer performance than the base fluid [8,9]. The dispersion of a small concentration of nanoparticles modifies the thermophysical properties of the base fluid [10]. Any solid nanostructured with the appropriate characteristics (thermal conductivity, chemical compatibility with the base fluid) can be dispersed into a base fluid. These nanostructures can be classified according to their nature in carbon-based nanostructures (carbon and graphite nanofibers, graphite nanoplatelets [11], graphene flakes [12]), carbon nanotubes (single- or multi-walled [13]), nanoparticles (ceramic [14,15], metallic [16], metallic oxides [17]) and nanowires (metallic [17], ceramic [17]). The volumetric fraction of nanoparticles can range from 0.1 to 6%; although, exceptionally some researchers have studied concentrations up to 10%. The utilization of nanofluids aims to increase the heat transfer coefficient of the flow, and achieve lower thermal losses and higher thermal efficiency.

Some of the key thermophysical properties of a nanofluid, or any fluid for this purpose are density, specific heat, thermal conductivity, and dynamic viscosity. Nanoparticles concentration affects the viscosity of the suspension and other thermal properties such as thermal conductivity or specific heat capacity. The amount of nanoparticles in the dispersion will define the nanofluids' performance. Thus, an optimal amount has to be used since it can represent the vast majority of the nanofluid production cost. An accurate understanding of the thermal behaviour of these materials through these properties is crucial to accomplish an optimal system design. Likewise, thermal conductivity and dynamic viscosity values have been proved difficult to determine through simple correlations [1]. Also, nanofluids usually exhibit complex rheological behaviour [18] with viscoelastic responses that should be thoroughly characterized, even for low nanoparticle contents. In this sense, Żyła founded non-Newtonian shear thinning behaviour for carbon

* Corresponding authors.
E-mail addresses: joseiglesias@uvigo.es (J.I. Prado), h.navarro@bham.ac.uk (M.E. Navarro).

https://doi.org/10.1016/j.molliq.2023.122293
Received 6 February 2023; Received in revised form 31 May 2023; Accepted 6 June 2023
Available online 12 June 2023

black nanoparticles in ethylene glycol for mass fractions upper than 0.25 wt% [19].

A special class of materials which take advantage of phase change to store large amounts of thermal energy is the so-called phase change materials (PCMs) [20]. Such materials have attracted significant interest in recent years from both academic and industrial communities as compact thermal energy storage materials [21]. Among PCMs, organic-based formulations are of specific interest due to non-toxicity, high latent heat, little sub-cooling, good chemical compatibility and recyclability [22]. Nanofluids based on PCMs are known as phase change nanofluids or nano-enhanced phase change materials (NePCMs) [23].

This work continues our previous research on the design, stability, characterization, and thermophysical properties of MgO nanoparticles and graphene nanoplatelets (GnP) suspended in PureTemp 8 (PT8), a stearate base fluid [24]. In the present paper, we present a study on the phase change characteristics, thermal diffusivity, and rheological behaviour of these nanofluids. The two types of nanoparticles studied are a metallic oxide (MgO) and a carbon-based material (graphene nanoplatelets). Magnesium oxide is one of the ceramic oxides that presents a high thermal conductivity (around 48 $W{\cdot}m^{-1}{\cdot}K^{-1}$) and low density (around 3.6 $g{\cdot}cm^{-3}$), when compared to other oxides such as Fe_2O_3, Fe_3O_4, ZnO, CuO or TiO_2 [25]. Graphene nanoplatelets or graphene flakes (GFs) are materials that contain between 10 and 30 honeycomb lattice sheets, a nanomaterial whose thickness is around 0.335 nm. These nanoplatelets present a high hydrophobicity, high thermal conductivity (between 3000 and 5000 $W{\cdot}m^{-1}{\cdot}K^{-1}$) and good electrical properties, suitable for electric applications [26]. The thermal and rheological properties of the nanofluids prepared with MgO (1.0, 5.0, 10, 15, 20, and 25 wt%) and GnP (0.25, 0.50, 0.75, 1.0 and 2.0 wt%) were studied using a Differential Scanning Calorimeter, Laser Flash Apparatus and a Rheometer. Comprehensive analysis of the results were carried out to understand the effect of the nanoparticles and their concentration on the thermal and rheological behaviour. These data will lead to encourage researchers to thoroughly characterize and design nanofluids to optimise their performance in energy applications.

2. Experimental

2.1. Materials

PureTemp 8 is a commercial PCM used in this work as the base fluid which was purchased from Entropy Solutions (Plymouth, USA). Spherical MgO nanoparticles (35 nm diameter) and graphene nanoplatelets (11–15 nm thickness) were provided by IoLiTec (Heilbronn, Germany) with mass purities of 99 and 99.5%, respectively. In our previous study on these nanofluids, we showed that the colloidal stability was improved by using acetic acid as the surfactant in acetic acid:nanoadditive mass rate of 0.75:1 [24]. Therefore, corresponding amounts of acetic acid from Sigma-Aldrich (St. Louis, USA) were added in the elaboration of the samples. Products were utilized as received without any additional purification.

NePCMs were elaborated following the procedure reported in our previous work [24]. Therefore, proper amounts of each component were weighed in an analytical balance Sartorius CPA225 (Göttingen, Germany) corresponding to the nanoparticle mass fractions (ϕ_m) that are indicated in Table 1 along with their correspondence into nanoparticle volume fraction (ϕ_v). An ultrasonic homogenizer Bandelin Sonopuls HD 2200 (Berlin, Germany), with a nominal power of 200 W and frequency of 20 kHz, was used to disperse the nanomaterials within the base PCM, keeping the samples soaked in an ice bath during this process.

2.2. Methods

The solid–liquid phase change transition was analysed in a Differential Scanning Calorimeter (DSC) TA Instruments Q2000 (New Castle, USA), equipped with a refrigerated cooling system RSC90. Samples were placed into hermetically crimped Tzero aluminium pans, which can withstand pressures up to 0.4 MPa. Tests were performed in a nitrogen atmosphere with a mole fraction purity higher than 0.99999 and at a flow rate of 50 $ml{\cdot}min^{-1}$. Four consecutive heating–cooling cycles from 250 to 320 K varying the heating rate at 1, 2, 5, and 10 $K{\cdot}min^{-1}$ were run on each sample without opening the DSC furnace. The expanded uncertainties ($k = 2$) for temperature and enthalpy are 0.3 K (with a repeatability of 0.1 K) and 1.2 $J{\cdot}g^{-1}$ (with a repeatability of 0.7 $J{\cdot}g^{-1}$), respectively [27].

Table 1
Nanoparticle mass fractions (ϕ_m) with their corresponding volume fractions (ϕ_v) of the prepared nanofluids.

MgO/PT8		GnP/PT8	
ϕ_m / wt%	ϕ_v / vol%	ϕ_m / wt%	ϕ_v / vol%
1.0	0.24	0.25	0.097
5.0	1.2	0.50	0.19
10	2.6	0.75	0.29
15	4.0	1.0	0.39
20	5.6	2.0	0.79
25	7.4		

Thermal diffusivity has been obtained through the Laser Flash Technique (LFA) with an LFA 427 apparatus (Netzsch) using a platinum crucible. The surface of the crucible was coated with a graphite layer, to increase the absorption and emission of radiation. The amount of sample used was 150 μl and the test was performed under 100 $ml{\cdot}min^{-1}$ nitrogen flow at 298.15, 323.15, 343.15, 363.15, and 393.15 K. The expanded uncertainty ($k = 2$) is 3% over the entire temperature range.

Rheological properties of the gathered nanofluids were obtained in an Anton Paar Physica MCR 101 (Graz, Austria) using a cone and plane geometry CP50-1 (50 mm diameter, 1° cone). The device allows to control the torque in the range from 0.5 to 125 mNm. A constant gap between the cone and the plate was kept at 102 μm. The temperature was kept at 283.15 K, being controlled by means of a Peltier system in the plate with an additional Peltier hood to assure a uniform temperature throughout the measuring gap. Also, prior to any test, aliquots of the samples of about 600 μl were rested in the plate during 300 s allowing time for temperature stabilization. Different experiments were carried out to perform a comprehensive rheological characterization of these PT8-based nanofluids, namely, flow tests and linear viscoelastic oscillatory measurements (strain and frequency sweeps). Rotational non-linear viscoelastic experiments measured the variation of the shear viscosity with increasing shear rates; flow tests were carried out from 0.1 to 10000 s^{-1}. Linear viscoelastic oscillatory tests were carried out to determine the linear viscoelastic regime (LVR) utilizing a strain sweep in which the store (G') and loss (G'') moduli were obtained at constant angular frequency $\omega = 10$ $rad{\cdot}s^{-1}$ in the strain range of 0.01 to 1000%. Then, frequency sweeps were performed at constant strain within the LVR, and an angular frequency varying from 600 to 0.1 $rad{\cdot}s^{-1}$. Three replicates at each experimental condition were accomplished to ensure the repeatability of the experiments. The expanded uncertainties ($k = 2$) of the torque and temperature are 1% and 0.06 K, respectively.

3. Results and discussion

3.1. Phase change characterization

Standard DSC measurements were carried out to explore the effect of dispersed MgO nanoparticles and GnP on the phase change characteristics of PT8 base fluid. Fig. 1 depicts the cooling and heating curves of the base PCM at various heating rates. This figure shows an exothermic event corresponding to the crystallization in every cooling curve and an endothermic event attributed to the melting for all heating curves. Different heating rates lead to a tiny shift in the solid–liquid transition temperatures, with maximum variations between extreme heating rates

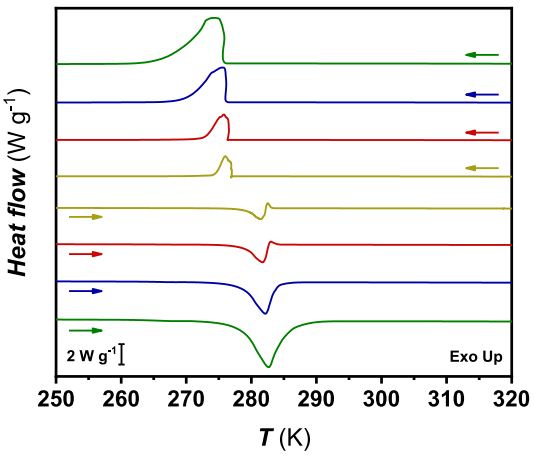

Fig. 1. Cooling and heating DSC curves of PT8 obtained at 10 K·min^{-1} (—), 5 K·min^{-1} (—), 2 K·min^{-1} (—), and 1 K·min^{-1} (—).

(1 and 10 K·min^{-1}) of 1.49 K in crystallization temperature and 1.31 K in melting temperature. In addition, a slightly decreasing trend of the latent heat with increasing heating rate was also found, up to 1.8% lower at 10 K·min^{-1} compared to 1 K·min^{-1}. Similar phase change behaviour was found by Yi *et al.* [28] for octyl, decyl, dodecyl, and tetradecyl stearates, which are PCMs of the same family as PT8 [24]. All these materials show similar DSC cooling and heating curves with one peak corresponding to the crystallization and another to the melting [28].

Fig. 2 illustrates the influence of the nanoparticle loading as well as the differences between the two types of used nanomaterials on the cooling and heating curves of the base PCM. These tests were performed at heating rates of 10 and 2 K·min^{-1}, the most commonly used in thermal analysis. All curves in Fig. 2 show the same exothermic event corresponding to the crystallization and the same endothermic event attributed to the melting, similar to those observed in the cooling and heating curves of the PT8 (Fig. 1).

Regarding nanodispersion samples, the additional exothermic recrystallization event can also be appreciated in the heating curves of both MgO and GnP-based nanofluids (Fig. 2a and 2c), suggesting a kinetic second-order phase change process of the base fluid that remains on the nanofluids. The latent heat decreases with the increasing nano-additive loading up to 27 and 7.6% for MgO/PT8 15 wt% and GnP/PT8 1.0 wt%, respectively. Regarding the influence of the heating rate on the solid–liquid phase change enthalpy, the higher the heating rate, the lower the latent heat for MgO/PT8 dispersions, whereas the opposite effect was found for GnP/PT8 NePCMs. This can be explained by the presence of a larger nucleating surface in GnP/PT8 than in MgO/PT8, due to the differentiated geometrical distribution and topography of the

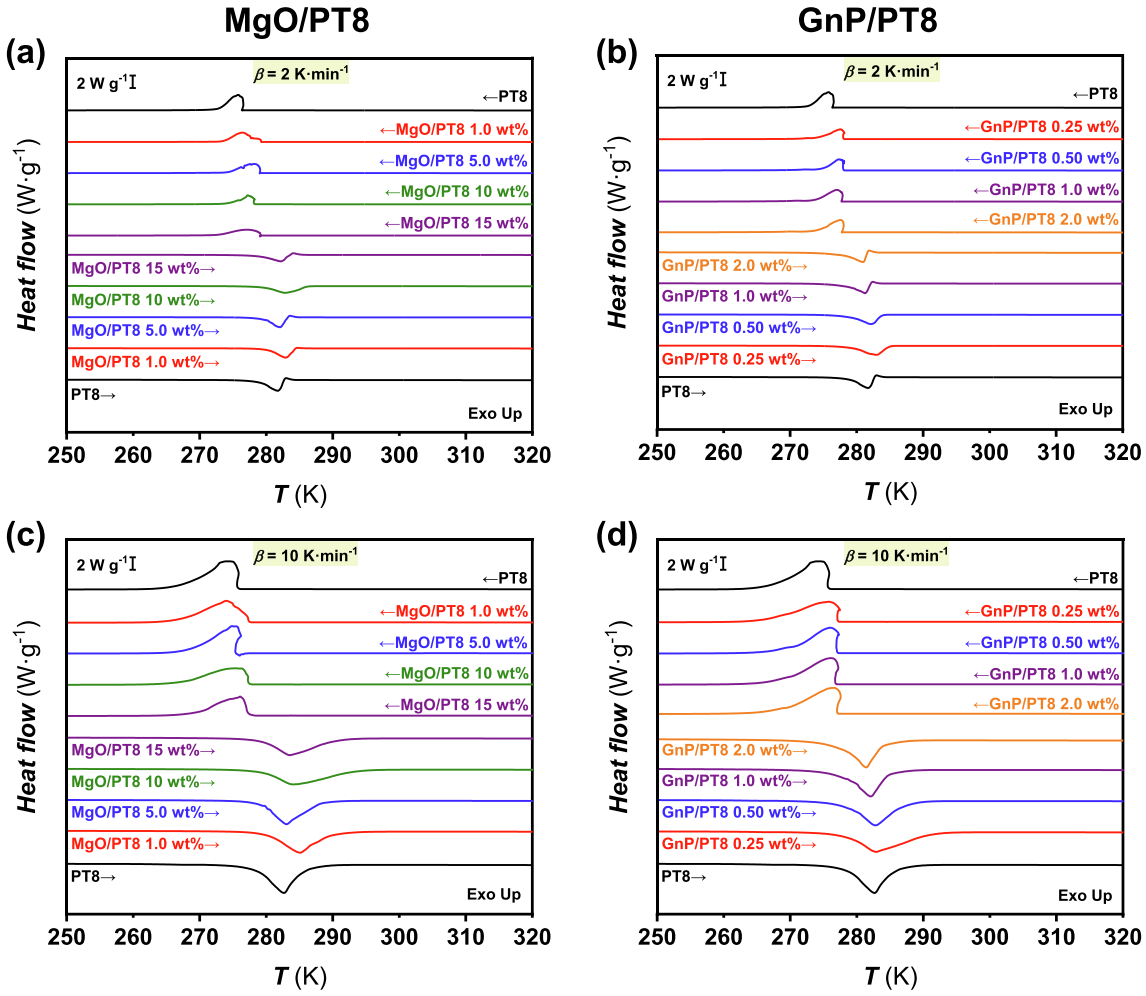

Fig. 2. Cooling and heating DSC curves of MgO/PT8 nanofluids at nano additive mass fractions of 0 wt% (—), 1.0 wt% (—), 5.0 wt% (—), 10 wt% (—), and 15 wt% (—), obtained at (a) 2 K·min^{-1} and (c) 10 K·min^{-1} and GnP/PT8 samples at mass fractions of 0 wt% (—), 0.25 wt% (—), 0.50 wt% (—), 1.0 wt% (—), and 2.0 wt% (—) obtained at (b) 2 K·min^{-1} and (d) 10 K·min^{-1}.

nanomaterials (sheets vs. spheres).

Small variations in the nanoadditive composition of the dispersions alter its melting and crystallization point [29], as can be seen in Table 2. The different nature of nanoparticles induces a change in the shape of the DSC curves of the base PCM that consequently modifies the values of the solidification and fusion heat and the melting and crystallization points of the NePCMs. Higher crystallization temperatures were obtained with the dispersion of GnP and MgO finding increases from 0.40 and up to 3.1 K. Regarding the melting point, the designed NePCMs behave differently; the dispersion of MgO nanoparticles increases the melting temperature of the PT8 from 0.26 and up to 2.3 K while the dispersion of GnP shows different effects depending on the mass concentration of the nanoplatelets. GnP/PT8 at 0.25 and 0.50 wt% show a slight mean increase of the melting point of 0.73 and 0.29 K respectively whereas mean decreases of the melting temperature of 0.52 and 0.96 K were found at 1.0 and 2.0 wt% respectively. Likewise, onset melting and crystallization temperatures decrease with the nanoadditive loading. The decrease is more noticeable in the case of GnP/PT8 crystallization, where onsets even disappear at 10 and 5 K·min^{-1} heating rates for all concentrations. This phenomenon is caused because, during the phase change, nanomaterials could serve as the core of crystal growth and they promote the crystal structure transformation.

It has been widely reported that high sub-cooling values hinder the utilization of PCM in TES systems due to the shift in the transition temperatures. The sub-cooling is usually defined as the difference between the melting and the crystallization temperature of the different samples. MgO/PT8 samples evidence sub-cooling values close to PT8 and even a slight decrease for all heating rates except for the 1.0 wt% mass concentration of MgO at 10 and 5 K·min^{-1}, as can be observed in Table 2, which shows an average increase of 2.5 K. The maximum sub-cooling reduction was found for MgO/PT8 5.0 wt% at 1 K·min^{-1} reaching decreases of 1.9 K.

Sub-cooling degrees of GnP/PT8 nanofluids are lower than those of PT8 for all analysed heating rates and the decrease is more noticeable with the increase in GnP content. This reduction goes from 0.10 to 3.4 K achieving the maximum decrease for GnP/PT8 2.0 wt% at 10 K·min^{-1}. This suggests that the dispersion of GnP is a more effective way to reduce the sub-cooling of PT8 compared to the use of MgO nanoparticles.

As an example, Fig. 3 depicts the solid–liquid phase change temperatures connected by a dropline that represents the sub-cooling at each studied mass fraction at 10 K·min^{-1}. The dispersion of the different nanomaterials into PT8 triggers distinctive effects on the sub-cooling. The sub-cooling of MgO/PT8 increases at 1.0 wt% and then slightly decreases with mass fraction, while there is a continuous decrease of the sub-cooling with increasing nanomaterial concentration for GnP/PT8.

The main phase change characteristics of the highest nanoadditive concentrations for the proposed NePCMs are shown in Fig. 4. To obtain these curves, enthalpy was determined following a similar procedure to

Table 2
Enthalpies of melting along with crystallization and melting temperatures of PT8 base fluid and GnP/PT8 and MgO/PT8 nanofluids.

ϕ_m (wt%)	β (K·min^{-1})	Cooling		Heating			Sub-cooling (K)
		T_{onset} (K)	T_{cryst} (K)	Δh_{melt} (J·g^{-1})	T_{onset} (K)	T_{melt} (K)	
PT8							
–	1	277.0	276.0	163.4	279.3	281.5	5.5
	2	276.6	275.8	163.3	279.0	281.8	6.0
	5	276.3	275.6	161.8	278.6	282.2	6.6
	10	–	274.5	160.4	278.4	282.8	8.3
MgO/PT8							
1.0	1	278.4	277.4	142.1	280.5	282.6	5.1
	2	279.2	276.4	143.0	280.2	282.9	6.5
	5	278.7	275.0	142.8	279.9	283.9	8.8
	10	277.4	274.0	140.9	280.1	285.1	11.1
5.0	1	279.4	279.1	151.6	280.5	282.8	3.7
	2	279.1	278.1	142.2	279.9	282.1	4.0
	5	277.9	276.7	139.8	279.7	282.6	5.9
	10	–	274.9	139.0	279.6	283.1	8.2
10	1	278.8	277.9	131.7	280.3	282.6	4.7
	2	278.1	277.2	133.0	279.5	282.7	5.6
	5	277.6	276.4	133.2	279.2	283.3	6.9
	10	277.3	275.4	135.0	279.2	284.1	8.7
15	1	278.9	278.0	117.4	278.8	281.9	4.0
	2	279.2	277.2	118.2	278.7	282.2	5.0
	5	277.6	276.7	119.7	279.3	282.9	6.2
	10	277.2	276.1	117.9	279.3	283.6	7.5
GnP/PT8							
0.25	1	278.3	277.7	157.6	282.0	282.7	5.0
	2	278.0	277.6	158.0	279.1	282.9	5.4
	5	–	276.1	159.5	278.7	282.6	6.5
	10	–	275.8	160.7	278.3	282.9	7.1
0.50	1	278.3	277.9	153.5	280.4	282.1	4.2
	2	278.0	277.4	152.7	278.9	282.2	4.9
	5	–	276.6	156.3	278.8	282.3	5.7
	10	–	276.0	152.4	278.4	282.8	6.8
1.0	1	278.2	277.3	151.0	279.0	281.1	3.8
	2	278.0	277.1	153.8	278.3	281.3	4.2
	5	–	276.7	158.5	278.9	281.7	5.0
	10	–	276.2	157.1	278.5	282.1	5.9
2.0	1	278.3	277.9	154.3	278.2	280.8	3.0
	2	–	277.6	158.6	277.7	281.0	3.3
	5	–	277.1	158.0	278.0	281.2	4.1
	10	–	276.5	161.9	277.9	281.4	4.9

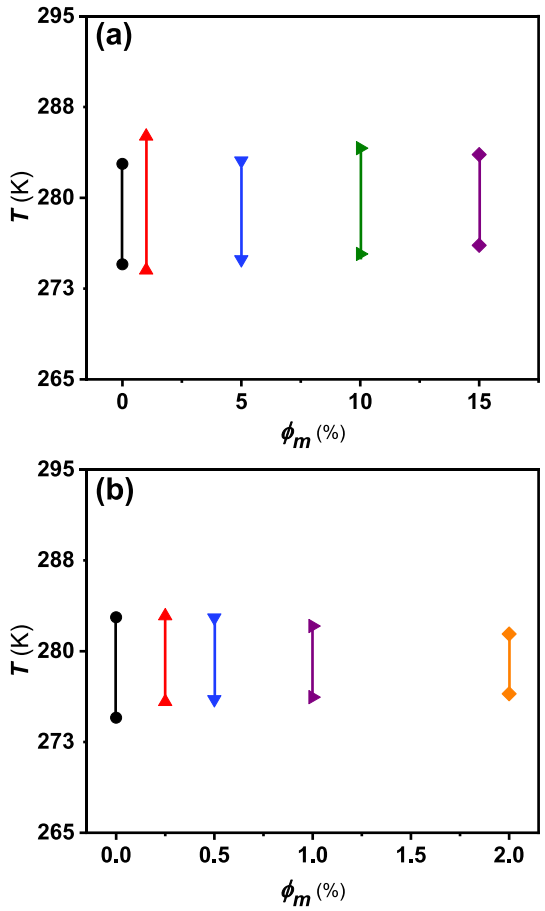

Fig. 3. Phase change temperatures as a function of the mass fraction of (a) MgO/PT8 and (b) GnP/PT8 NePCMs at 10 K min^{-1}. Droplines represent sub-cooling.

the one proposed by Vélez *et al.* [30] from the thermograms at 10 K·min^{-1} and the isobaric heat capacity data from our previous study [24]. All curves show the solid and the liquid region where the enthalpy slightly increases with temperature and a transition region between the formers where the phase change takes place and a noticeable and rapid augmentation of the enthalpy is registered.

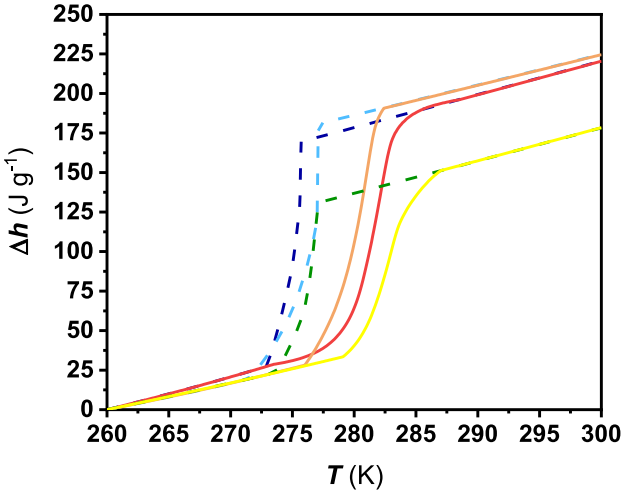

Fig. 4. Enthalpy-temperature curves (dash line for cooling and solid line for heating) of PT8 (cooling - - - & heating ——), MgO/PT8 15 wt% (cooling - - - & heating ——), and GnP/PT8 2 wt% (cooling - - - & heating ——) obtained at heating rate of 10 K·min^{-1}. Reference state: $\Delta h = 0$ at 260 K.

In Fig. 4, noteworthy differences are shown concerning the phase change characteristics of MgO/PT8 15 wt% and GnP/PT8 2.0 wt%. The latent heat of MgO/PT8 15 wt% decreases by 27% while increasing 0.94% for GnP/PT8 2 wt% compared to PT8. The variation of the crystallization temperatures of these NePCMs compared to the base PCM can also be inferred from Fig. 4. The transition region is defined by two temperatures, one at which starts (onset point) and one at which ends (offset point). For cooling curves, the onset is higher than the offset, while for heating curves is just the opposite. The phase change temperature (either melting or crystallization) is located at the mean height of the transition region of the heating/cooling curve, as reported in Table 2 in Fig. 4.

3.2. Thermal diffusivity

Currently, there is no mathematical model that can predict the anomalous thermal conductivity variation of nanofluids [31]. Researchers found, from experimental results, that nanofluids' thermal conductivity (thermal diffusivity) depends on several parameters such as the base fluid properties, the nanoparticles' characteristics (volume fraction, surface area, shape, and chemical composition), and the working conditions. In addition, the methods used to perform these measurements, transient methods like hot wire or laser flash apparatus, have their own inherent technique/instrument error associated, which leads to scattered data [31]. Thus, comparing the values in these studies is difficult, also to reproduce them.

The results of the thermal diffusivity versus temperature and mass fraction using the LFA apparatus of MgO/PT8 and GnP/PT8 nanofluids are shown in Fig. 5. In both cases, it can be seen that GnP suspensions do not show any apparent trend, whereas MgO/PT8 suspensions show an increase in thermal diffusivity with MgO content. However, the uncertainty of the values can, in some cases overlap the achieved enhancement. The uncertainty of the measurements is much higher at room temperature. One of the reasons is that the detector is not very sensitive at room temperature and the signal amplifier gain and orifice setting of the InSb detector work at their maximum to achieve the biggest signal possible. It can be seen that as soon as the temperature increases the sensitivity of the detector improves and the thermal diffusivity values error decrease substantially. When comparing MgO and GnP suspensions, it can be seen that GnP samples reach higher thermal diffusivity values than MgO, with lower nanoadditive content, due to the differences in thermal conductivity values of the raw materials. However, the dispersion of the results is higher in GnP suspensions, which could be attributed to the stability of the suspensions at higher temperatures.

Nanofluids stability is one of the key problems that substantially impacts their applicability, as it affects the NePCMs' properties. The nanoparticles' agglomeration and settlement can reduce the nanofluid's thermal conductivity, as already several researchers observed [32]. Understanding and controlling the stability of nanofluids' dispersions over their working temperature range and chemical conditions are two key aspects for its successful application. In our previous work, we have reported an improvement in the temporal stability of these NePCMs due to the existence of some disaggregation phenomena of the initial clusters of nanoadditives [24]. Wang and Guo [33] already observed that temperature had a strong destabilizing effect on nanofluids' suspensions. In Fig. 5 the thermal diffusivity enhancement of the prepared samples is compared versus concentration. During LFA measurements the samples are studied in static conditions, with no external forces applied, achieving more stable suspensions for MgO/PT8 than GnP/PT8.

3.3. Rheological behaviour

3.3.1. Non-linear viscoelastic experiments

Different nanoadditive mass fractions of each nanofluid set were taken into account to analyse the effect of the concentration of the dispersed nanomaterial on the rheological properties of the gathered

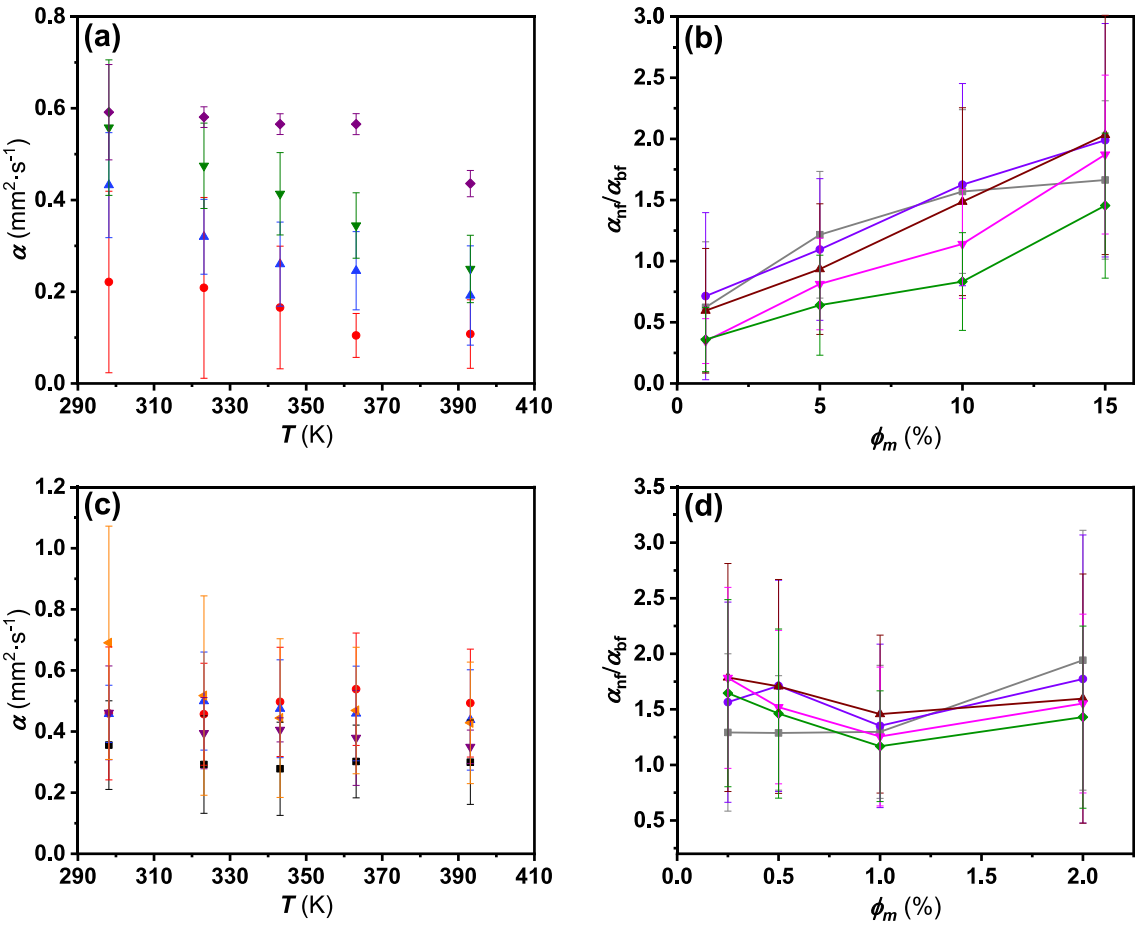

Fig. 5. (a) Temperature dependence on thermal diffusivity of MgO/PT8 NePCMs at mass fractions of 1.0 wt% (●), 5.0 wt% (▲), 10 wt% (▼), and 15 wt% (◆). (b) Thermal diffusivity enhancement as function of the mass fraction of MgO/PT8 at temperatures: 298.15 K (■), 323.15 K (●), 343.15 K (▲), 363.15 K (▼), and 393.15 K (◆). (c) Temperature dependence on thermal diffusivity of GnP/PT8 NePCMs at mass fractions of 0.25 wt% (●), 0.50 wt% (▲), 1.0 wt% (◆), and 2.0 wt% (◀). (d) Thermal diffusivity enhancement as function of the mass fraction of GnP/PT8 at temperatures: 298.15 K (■), 323.15 K (●), 343.15 K (▲), 363.15 K (▼), and 393.15 K (◆).

nanofluids. Fig. 6 shows the flow curves for MgO/PT8 and GnP/PT8 nanofluids. The PT8 base fluid is $\dot{\gamma}$-independent demonstrating Newtonian behaviour, therefore it is defined as a unique shear viscosity for all studied shear rates at each temperature. On the other hand, nanofluids exhibit shear-thinning (pseudoplastic) non-Newtonian behaviour with yield stress (viscoplastic behaviour, *i.e.*, solid-like when stationary) in case MgO/PT8 NePCMs and without yield stress (viscoelastic behaviour, *i.e.*, liquid-like when stationary) for GnP/PT8 samples. The main difference between shear-thinning behaviour with or without yield stress is the presence of a Newtonian plateau in the lowest $\dot{\gamma}$ region, known as zero shear viscosity (η_0), in the former while in the latter there is an infinite asymptotic behaviour when approaching zero-shear rate. As observed in Fig. 6a, shear viscosity continuously decreases as $\dot{\gamma}$ increases according to a shear-thinning power-law behaviour for MgO/PT8 NePCMs, whereas in Fig. 6b a Newtonian plateau at the lowest $\dot{\gamma}$ is observed for GnP/PT8.

In the highest $\dot{\gamma}$ region is possible to observe another Newtonian plateau, in both MgO and GnP-based nanofluids, which is used to be identified as a limiting viscosity, known as infinite shear viscosity (η_∞). As nanoadditive concentration increases, this Newtonian plateau is reduced, indicating that the shear-thinning effect is more noticeable. This shear-thinning effect has also been observed by Esfe and Mosaferi [34] for MgO/5w30 engine oil dispersions, Yapici *et al.* [35] for MgO/ethylene glycol nanofluids, Demirkır and Ertürk [36] for graphene/water nanofluids, and Vallejo *et al.* [37] for graphene nanoplatelet nanofluids based on water and propylene glycol: water mixtures at 30:70 and 50:50 wt%.

Many materials exhibit a threshold stress which must be exceeded to allow flowing, so-called yield stress (τ_y). When the applied local shear stress is below the yield stress ($\tau < \tau_y$), the material absorbs the stress-energy, showing no deformation (or flowing), and thus, behaving like a solid. Once this threshold is exceeded ($\tau > \tau_y$), significant deformation in the material is observed and, indeed, it flows like a liquid, following a shear thickening or shear-thinning non-linear relationship. This behaviour is observed in Fig. 6c for MgO/PT8 nanofluids and can be associated with the reorientation of the nanoparticles (and/or aggregates) when increasing the applied shear stress over the yield stress. The Herschel-Bulkley model [38], a modification of the Ostwald-de Waele relationship incorporating yield stress, was used to correlate the relationship between τ and $\dot{\gamma}$ in MgO/PT8 nanofluids. This model can be expressed as follows

$$\tau = \tau_y + k\dot{\gamma}^n, \tag{1}$$

where τ_y is the dynamic yield stress, k the consistency index, and n the power-law index. If $n = 1$ the model reduces to Bingham's while if, in addition, there is no yield stress ($\tau_y = 0$), the model reduces to Newtonian's. Also, the power-law index indicates if the fluid is shear thinning ($n < 1$) or shear thickening ($n > 1$). Table 3 encloses the fitted parameters of equation (1) for MgO/PT8 nanofluids at each studied mass fraction along with the standard deviations. All the obtained

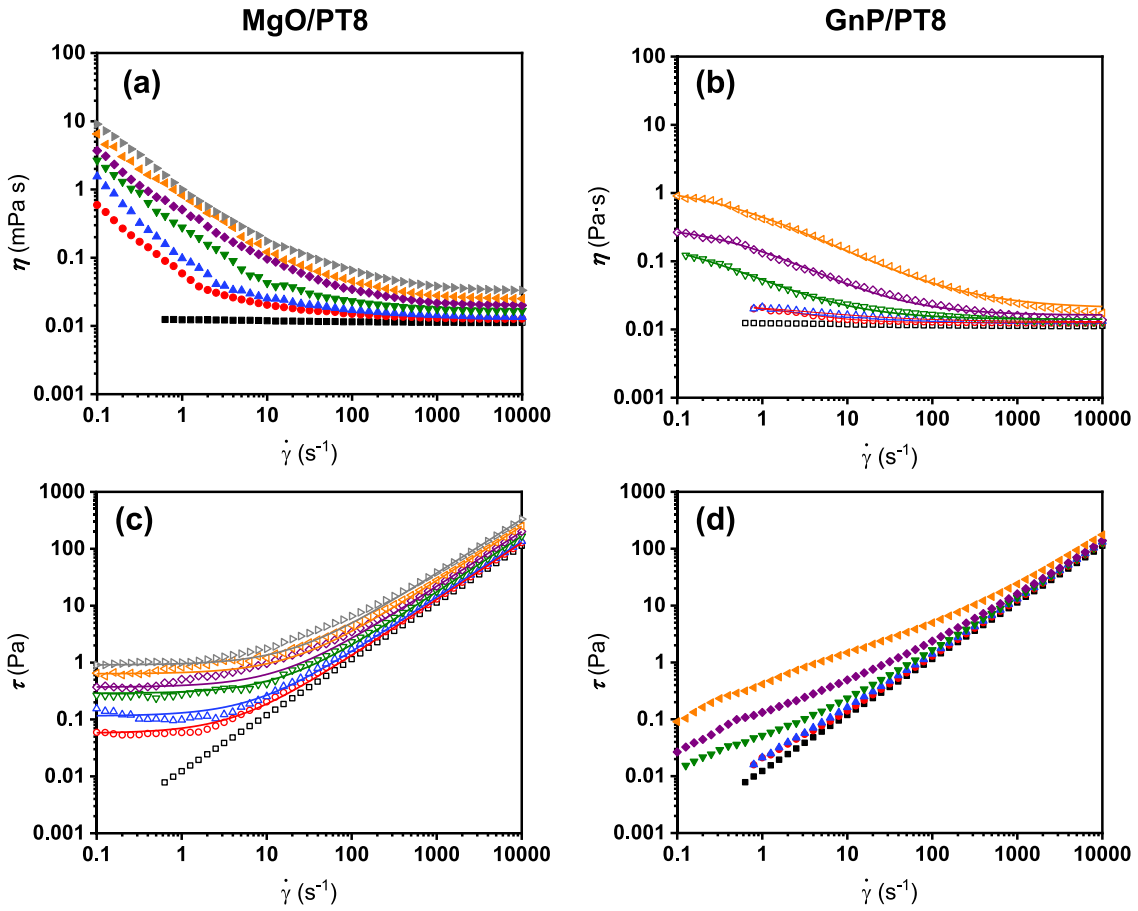

Fig. 6. Shear viscosity (η) and shear stress (τ) as function of the shear rate at 283.15 K for (a,c) MgO/PT8 NePCMs at mass fractions of 0 wt% ((■/□)), 1.0 wt% (●/○), 5.0 wt% (▲/△), 10 wt% (▼/▽), 15 wt% (◆/◇), 20 wt% (◀/◁), and 25 wt% (▶/▷) and (b,d) GnP/PT8 NePCMs at mass fractions of 0 wt% (□/■), 0.25 wt% (○/●), 0.50 wt% (△/▲), 0.75 wt% (▽/▼), 1.0 wt% (◇/◆), and 2.0 wt% (◁/◀). Lines refer to the fitting according to the Herschel-Bulkley model, eq. (1), (c) and to the Cross model, eq. (2), (b).

power-law indices are lower than 1, which indicates shear thinning, in agreement with the observed behaviour in Fig. 6c. Also, n slowly decreases with the mass fraction, while the dynamic yield stress rapidly grows with the loading of dispersed MgO nanoparticles. It must be mentioned that the augmentation on the standard deviation with increasing mass fraction reported in Table 3 comes from the increasing order of magnitude of the measured stresses, as can be observed in Fig. 6c.

On the other hand, GnP/PT8 nanofluids were modelled by using the Cross model [39], which is suitable for materials showing two limiting viscosities (η_0 and η_∞), as these nanofluids exhibit:

$$\frac{\eta-\eta_\infty}{\eta_0-\eta_\infty}=\frac{1}{1+K\dot{\gamma}^n}, \tag{2}$$

where K is the time constant that controls the breakdown of the viscosity and n is the aforementioned power-law index. The obtained parameters in the fitting of the Cross model for GnP/PT8 nanofluids have been enclosed in Table 4. As equation (2) is not applicable to Newtonian fluids, samples at 0.25 and 0.50 wt% (the lowest mass fractions) cannot be modelled this way, and, accordingly, have not been included in this table. Both limiting viscosities increase with the mass fraction, while the power-law index and the time constant get reduced with the GnP loading. Similar to MgO-based NePCMs, all the obtained n values for GnP/PT8 nanofluids are lower than 1, indicating shear thinning, in agreement with the observed behaviour in Fig. 6b. As above-mentioned for MgO/PT8 dispersions, the standard deviation for this model also increases with the mass fraction, coming to this effect also from the higher measured viscosities, as can be seen in Fig. 6b.

Although the use of viscometers is common in the nanofluid literature, it should be mandatory to perform rheological tests instead of assuming Newtonian behaviour when studying nanostructured fluids, as here reported results reveal and as previously reported [40]. The shear-thinning effect for MgO/PT8 and GnP/PT8 nanofluids is related to internal structural modifications and rearrangements of the interacting particles [41]. At rest, MgO nanoparticles and GnPs are randomly disordered in the PT8 base fluid due to the domination of the Brownian movement and van der Waals forces contribute to the formation of agglomerates [42]. The combination of these two differentiated effects leads to high resistance to flow, and therefore, large viscosity values at the lowest shear rates, as depicted in Fig. 6. Shearing induces the reorientation of the particles in the direction of flow that breaks the

Table 3
Dynamic yield stress (τ_y), consistency index (k), power-law index (p), and standard deviations (σ) from Herschel-Bulkley model (eq. (1)) for MgO/PT8 nanofluids.

ϕ_m / wt%	1.0	5.0	10	15	20	25
τ_y / Pa	0.0571	0.115	0.287	0.369	0.634	0.907
k / Pa·s^p	0.0132	0.0160	0.0190	0.0270	0.0346	0.0499
p	0.996	0.981	0.985	0.967	0.965	0.954
σ / Pa	0.0025	0.021	0.030	0.069	0.084	0.14

agglomerates and accordingly the viscosity of the nanofluid is reduced.

3.4. Linear viscoelastic oscillatory tests

The viscoelasticity of the nanofluids was investigated using a dynamic technique, through oscillatory experiments, in which a sinusoidal stress is applied to the sample whose response (strain) will be generally shifted by a phase angle with respect to the strain wave. This allows to separate the stress into two components: one in phase with the strain, the elastic contribution (τ'), and the other out of phase with the strain, the viscous contribution (τ"). From these two components, the elastic or storage modulus G' and the viscous or loss modulus G" can be easily derived.

The first set of tests, strain sweeps at constant angular frequency $\omega = 10$ rad·s^{-1}, allowed us to identify the linear viscoelastic region (LVR). Fig. 7 encloses both storage and loss moduli as function of the strain deformation for the studied dispersions. Concerning MgO/PT8 nanofluids, in this linear regime, both moduli are constant regardless of strain amplitude up to a critical strain (γ_c) whence monotonically decrease at high strains, exhibiting an overshoot phenomenon of G" over G' (G" > G' at high strains, as can be seen in Fig. 7). The interpretation of this effect is that when an external strain is applied to these nanofluids, the material absorbs the deformation up to γ_c from which MgO nanoparticles and existing aggregates at rest begin to disaggregate. Thus, the structure losses strength becomes more liquid-like (G" dominates over G'). On the contrary, there is a slight domination of G" over G' throughout the entire measured strain amplitude range for GnP/PT8 nanofluids. Therefore, these nanofluids are liquid-like independent of the applied deformation. Even more, G' is zero for any applied strain for the lowest concentrated GnP-based nanofluids (0.25 and 0.50 wt%). This indicates that there is no elasticity in these samples, acting like a Newtonian fluid, as also shown in Fig. 7.

Both moduli G' and G" for MgO-based NePCMs are about 3 orders of magnitude larger than for GnP-based ones. This remarkable difference evidences the stronger structure that exists in MgO/PT8 compared to GnP/PT8 nanofluids, which may be due to the size difference between these two kinds of nanomaterials. Since MgO nanoparticles are spherical and with a nominal diameter of 35 nm can easily be surrounded and stabilized by the molecules of the base fluid forming a more gel-like structure than in the case of GnP, in which the sheet shape prevents this accommodation for the same mass fractions and so, leading to a more fluid behaviour of the system.

These effects can be easily observed by examining the evolution of the phase angle δ with the applied stress, δ being the shift between the wave of the perturbation (stress) and that of the material response (strain), which can be computed from tan δ = G"/G'. Phase angle values range from 0° to 90°, whose extremes correspond to ideal elastic solid and ideal viscous liquid behaviour, respectively. Between both of them, it is possible to differentiate two zones, one where elasticity domains viscosity ($G' > G''$) in which the material behaves as a viscoelastic solid (gel-like state), and another where viscosity domains elasticity ($G' < G''$) in which the material acts as a viscoelastic liquid (fluid state). The transition, $G' = G''$, corresponding to a phase angle of 45°, is usually referred to as the gel point. In Fig. 8 the phase angle of the different studied nanofluids is represented as a function of the applied strain deformation.

All MgO/PT8 nanofluids evolve from a gel-like state at rest (low strains) to a fluid state (high strains), reaching the ideal viscous liquid state when approaching 1000% of deformation. On the contrary, GnP/PT8 nanofluids at mass fractions of 0.25 and 0.50 wt% act as an ideal viscous liquid for all the studied strain deformations range, which is in line with the flow results discussed in the last section. At higher mass fractions of GnP, nanofluids behave as non-ideal fluids above the gel point, except 2.0 wt% which modestly reaches the gel point at 0.5% of applied strain.

To further characterize the well-defined LVR of MgO/PT8 nanofluids, shear stress–strain curves were also plotted in Fig. 9a for all studied concentrations of nanoparticles. The loss of linearity allows the determination of the static yield stress (τ_0) along with the associated critical strain (γ_c), these values being summarized in Table 5. As shown in Fig. 9b, static yield stress exponentially increases with the volumetric fraction of MgO nanoparticles whereas critical strains go from 0.126% for the lowest concentrations to 0.1% for the highest concentrations.

Particles in a colloidal suspension form aggregates that constitute a porous network within the continuous phase [43]. The competition between Brownian diffusion, intermolecular forces and gravity force might lead to the aggregation and/or the sedimentation of the nanoparticles. Since nanoparticles are always moving within the fluid, nanoparticles tend to collide with each other, forming a network of aggregates thanks to van der Waals interactions [44]. Therefore, the dynamics of the nanoparticles can be explained in terms of the geometry of the gel network of nanoparticles [43]. Rheological properties are directly related to the structure of the aggregated network, which can be described by fractal analysis, as reported by Shih *et al.* [45]. The determination of the structure of the network from rheological data needs a model that relates the viscoelastic properties with the geometrical parameters: a so-called scaling theory. Shih *et al.* [45] developed a scaling model that relates G' with the volume fraction utilizing a power relationship. A fractal pattern or set is characterized by an index that quantifies its complexity, commonly known as fractal dimension, with Hausdorff dimension (d_f) being the most popular [46]. It is rarely an integer number that constitutes a generalization of the dimension of a real vector space (commonly, Euclidean or topological dimension) based on the measurement of the local size of a set. The value of d_f determines the ability of a structure to fill the available space. The analysis of the fractal dimension gives relevant information about the geometrical aspects of the nanofluid as well as helps in the identification of the aggregate mechanism. Shih *et al.* [45] described the relationship between the static yield stress of the suspension, τ_0, and the volume fraction of nanoparticles, which can be expressed in a simplified form as follows:

$$\tau_0 = a\,\phi_v^m, \tag{3}$$

where a is a parameter that depends on the size of the nanoparticles, the interparticle average distance and the zeta potential of the suspension whereas $m = (d + X)/(d - d_f)$, d is the Euclidean dimension (in this case $d = 3$), X being the aggregate backbone dimension of the clusters, and d_f being the fractal dimension. The fitting to the experimental data enclosed in Fig. 9b allows us to obtain $m = 2.1 \pm 0.3$. Thus, this value yields to the fractal dimension of 1.1, assuming an aggregate backbone dimension $X = 1$ due to the abundance of chain-like aggregates forming dendrites. This aggregate backbone dimension lies in the Euclidean extremes of a line ($d = 1$) and a plane ($d = 2$), indicating the existence of a two-dimensional porous structure in MgO/PT8 nanofluids. The aggregation mechanisms of any colloidal system are regulated by the balance between attractive and repulsive forces, that are characterized by a certain potential. These potentials can be described by means of the well-known Derjaguin-Landau-Verwey-Overbeek (DLVO) theory [47]. Classically, two limiting regimes are distinguished, diffusion-limited

Table 4
Zero shear viscosity (η_0), infinite shear viscosity (η_∞), time constant (K), power-law index (n), and standard deviations (σ) from the Cross model (eq. (2)) for GnP/PT8 nanofluids.

ϕ_m / wt%	0.75	1.0	2.0
η_0 / Pa·s	0.227	0.336	1.32
η_∞ / Pa·s	0.0141	0.0162	0.0204
C / s	14.0	2.30	4.95
n	0.749	0.768	0.673
σ / Pa	0.00020	0.00067	0.0023

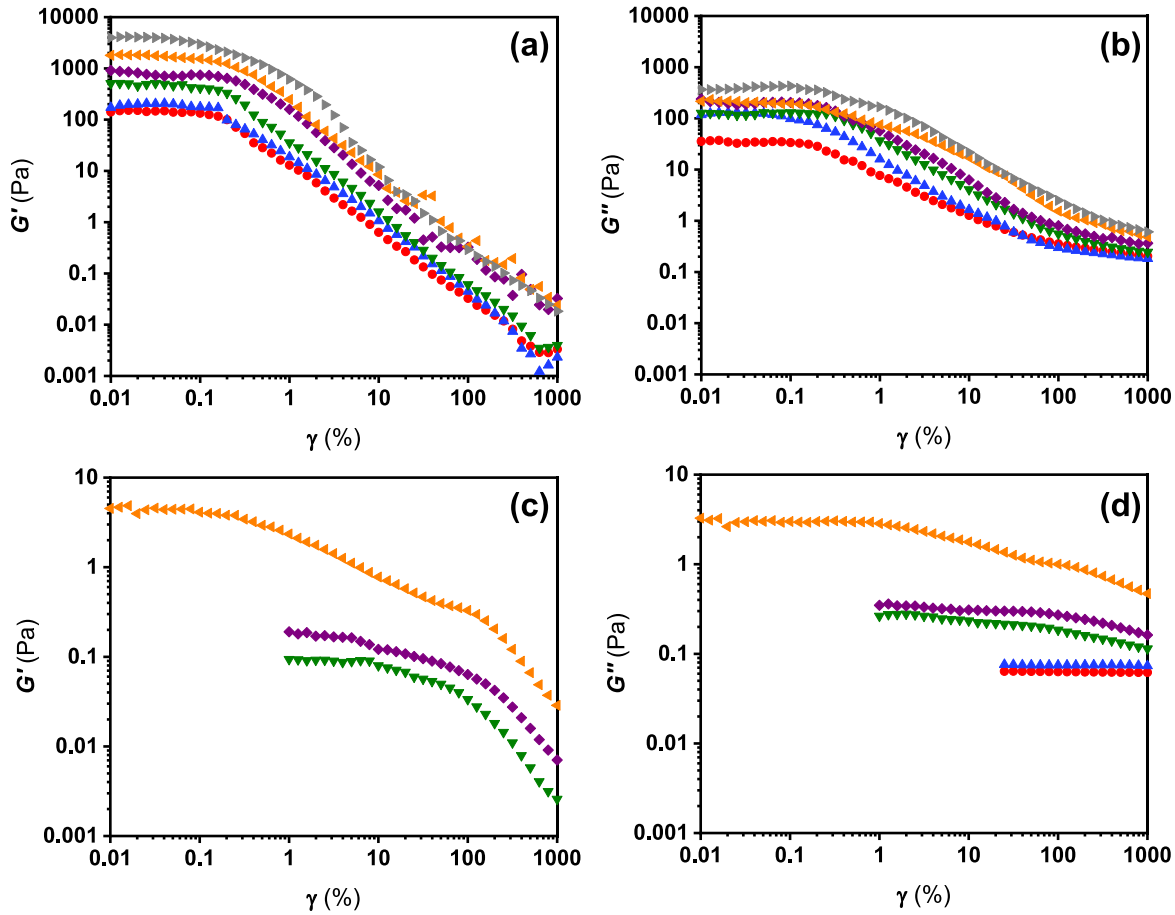

Fig. 7. Storage (*G'*, left charts) and loss moduli (*G''*, right charts) as a function of strain at 283.15 K and 10 rad·s^{-1} for (a,b) MgO/PT8 nanofluids at mass fractions of 1.0 wt% (●), 5.0 wt% (▲), 10 wt% (▼), 15 wt% (◆), 20 wt% (◀), and 25 wt% (▶) and (c,d) GnP/PT8 nanofluids at mass fractions of 0.25 wt% (●), 0.50 wt% (▲), 0.75 wt% (▼), 1.0 wt% (◆), and 2.0 wt% (◀).

cluster aggregation (DLCA) and reaction-limited cluster aggregation (RLCA), whose characteristic d_f values were established as 1.8 and 2.1, respectively [48]. The obtained d_f of 1.1 is far from those limiting regimes, suggesting that the formed clusters in MgO/PT8 are not compact with the presence of long-range attraction forces [47].

Moreover, the strength of the structure of the nanofluid was also characterized by means of the cohesive energy density, E_c, which can be derived as follows [49]:

$$E_c = \int_0^{\gamma_c} \tau \, d\gamma, \tag{4}$$

in which γ_c is the critical strain, which can be obtained from Table 5, and τ the applied stress. Since the cohesive energy is calculated in the LVR, as can be seen in the limits of the integral in equation (4), the shear stress can be obtained from the fact that in the linear range where $\tau = G_0'\gamma$, stands for the zero-shear elastic modulus. Thus, the following equation is obtained by computing the integral:

$$E_c = \frac{1}{2}\gamma_c^2 G_0', \tag{5}$$

The cohesive energy density takes into account the deformability of the structure throughout the critical strain [50]. Also, E_c is the threshold energy that represents the work needed to trigger the breakdown of the nanostructure. The cohesive energy density exponentially increases with volume fraction for MgO/PT8 nanofluids, as shown in Table 5, in a similar way to the static yield stress. This is a direct consequence of the reduction in the interparticle distance with the increasing volume fraction of MgO nanoparticles.

The second set of linear viscoelastic oscillatory tests consists of frequency sweeps at constant strain within the LVR. According to this criterion, MgO/PT8 samples were tested at a strain of 0.1% while GnP/PT8 nanofluids were measured at 5% for 0.25, 0.50, 0.75, and 1.0 wt% and 0.1% for 2 wt%. Fig. 10 shows the experimental data of storage (*G'*) and loss (G") moduli as a function of the angular frequency.

For MgO/PT8, the storage modulus exceeds the loss one ($G' > G''$) overall in the whole studied ω range, indicating the domination of the elastic nature in the material which behaves in a gel-like state. On the contrary, the opposite results were obtained ($G' < G''$) for all angular frequencies at mass fractions up to 1.0 wt% for GnP/PT8. The highest studied mass fraction, 2.0 wt% exhibits a gel point threshold ($G' = G''$) at $\omega \approx 20$ rad·s^{-1}, *i.e.*, at a lower angular frequency, whereas the storage modulus dominates at a higher angular frequency, the loss modulus preponderates. Therefore, the behaviour of the material shifts from a gel-like state at low angular frequencies (long-term behaviour) to a fluid state at high angular frequencies (short-term behaviour).

The difference in moduli values for MgO and GnP-based nanofluids is not as large as the above-mentioned for the strain sweeps, in this case being around one order of magnitude. The most remarkable difference in the behaviour of both NePCMs is the existence of a *G'* plateau in MgO/PT8, which is associated with the strength of the MgO network [51], that has been not observed for GnP/PT8 samples at mass fractions up to 1.0 wt%. Although, for the highest concentration of GnP (2.0 wt%) a plateau is observed, its strength is more reduced than those for MgO-based

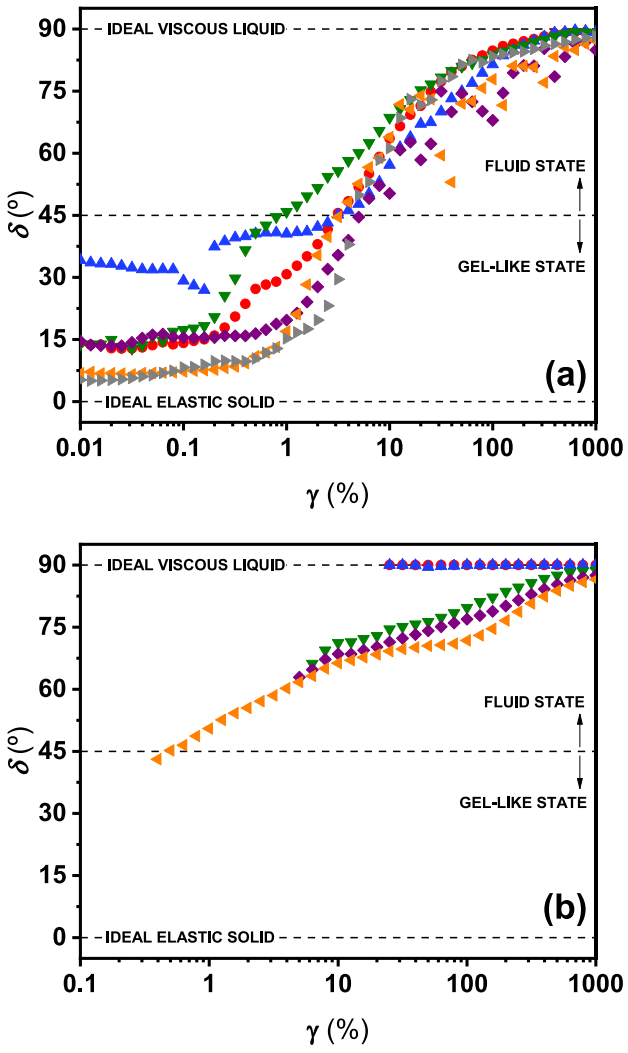

Fig. 8. Phase angle as a function of strain at 283.15 K and 10 rad·s^{-1} for (a) MgO/PT8 nanofluids at mass fractions of 1.0 wt% (●), 5.0 wt% (▲), 10 wt% (▼), 15 wt% (◆), 20 wt% (◀), and 25 wt% (▶) and (b) GnP/PT8 nanofluids at mass fractions of 0.25 wt% (●), 0.50 wt% (▲), 0.75 wt% (▼), 1.0 wt% (◆), and 2.0 wt% (◀). Classical extremes (ideal elastic solid and ideal viscous liquid) along with the ranges for fluid and gel-like states are indicated.

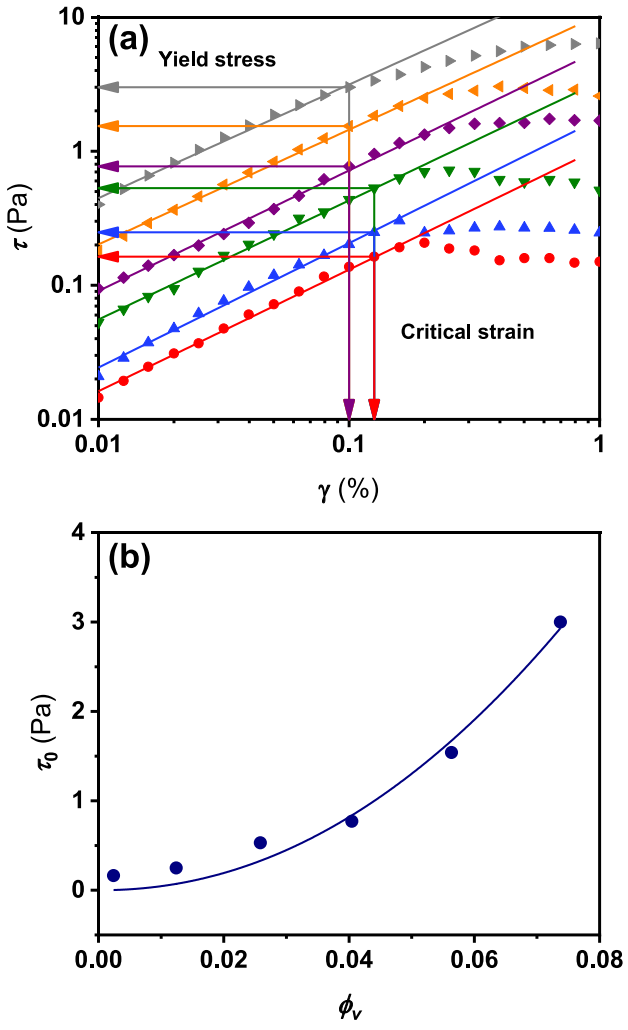

Fig. 9. (a) Shear stress versus strain at 283.15 K and 10 rad·s^{-1} for MgO/PT8 nanofluids at mass fractions of 1.0 wt% (●), 5.0 wt% (▲), 10 wt% (▼), 15 wt% (◆), 20 wt% (◀), and 25 wt% (▶). Lines are used as a guidance to identify the static yield stress and the critical strain, (b) Static yield stress as function of the nanoparticle volume fraction for MgO/PT8 nanofluids. Solid line refers to the fitting according to eq. (3).

nanofluids ($G'_{GnP} < G'_{MgO}$). Thus, a lower GnP concentration leads to the extinction of the gel network. In addition, the percolation nanoparticle volume fraction for MgO/PT8 NePCMs was obtained by means of the relationship between G'_0 and ϕ_v [52]:

$$G'_0 \propto (\phi_v - \phi_{v,0})^V, \quad (6)$$

where $\phi_{v,0}$ is the percolation volume fraction, *i.e.*, a threshold that indicates the volume fraction from which the gel network is created. For MgO/PT8 nanofluids, a close-to-zero critical concentration was found, which is in agreement with the previously discussed behaviour of these samples, which have evidenced a solid-like behaviour at rest. Therefore, all tests here reported, non-linear viscoelastic and linear viscoelastic oscillatory tests, were performed beyond this threshold, in a gel-like state. This fact indicates that the van der Waals forces are so strong that even very low concentrations induce the formation of a gel structure.

Table 5
Static yield stress (τ_0), critical strain (γ_c) and cohesive energy density (E_c) obtained from equation (5) for MgO/PT8 nanofluids at 283.15 K and different nanoparticle volume fractions.

ϕ_v	0.0024	0.012	0.026	0.040	0.056	0.074
τ_0 / Pa	0.163	0.248	0.530	0.771	1.54	3.00
γ_c / %	0.126	0.126	0.126	0.100	0.100	0.100
E_c / J·m^{-3}	0.11	0.15	0.38	0.39	0.86	1.89

4. Conclusions

We have presented a comprehensive thermal and rheological analysis of two sets of nanofluids based on dispersions of either MgO spherical nanoparticles or graphene nanoplatelets in PureTemp 8 (PT8). Some feedback for the application of these featured new materials in thermal energy storage systems can be drawn:

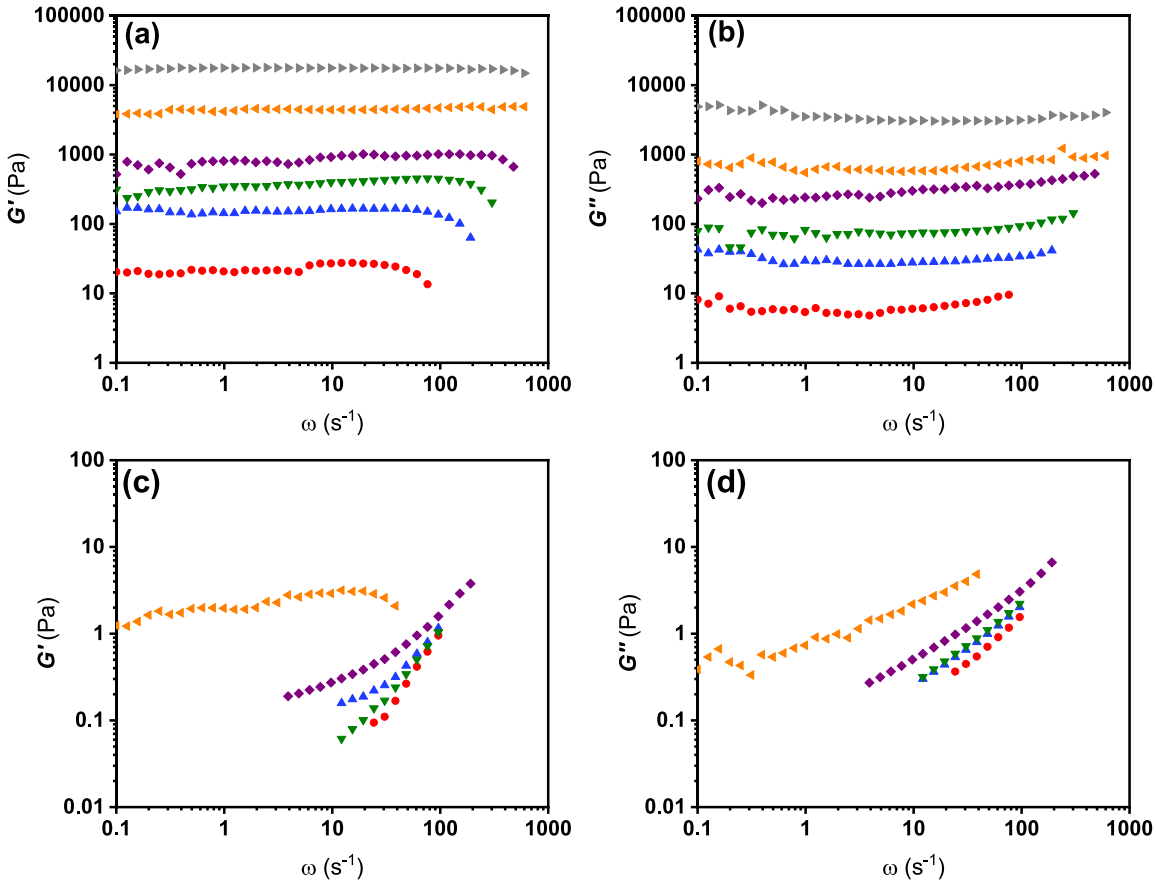

Fig. 10. Storage (*G'*, left charts) and loss moduli (*G''*, right charts) as a function of angular frequency at 283.15 K for (a,b) MgO/PT8 NePCMs at constant strain of 0.1% for mass fractions of 1.0 wt% (●), 5.0 wt% (▲), 10 wt% (▼), 15 wt% (◆), 20 wt% (◀), and 25 wt% (▶) and (c,d) GnP/PT8 NePCMs at constant strain of 5% for nanoadditive mass fractions of 0.25 wt% (●), 0.50 wt% (▲), 0.75 wt% (▼), 1.0 wt% (◆), and at constant strain of 0.1% for nanoadditive mass fraction of 2.0 wt % (◀).

- The dispersion of nanomaterials within PT8 does not alter the phases behaviour of the samples, which exhibit a clear first-order solid–liquid phase transition corresponding to the melting (heating) and crystallization (cooling) processes. Latent heat decreases for both MgO/PT8 and GnP/PT8 nanofluids up to 27% (15 wt%) and 7.6% (1.0 wt%), respectively. Likewise, transition temperatures shift with the dispersion of both nanomaterials, this effect being in benefits of the samples by reducing their sub-cooling.
- The dispersion of both nanomaterials into the PT8 base fluid affects the thermal diffusivity values; in both cases, there is an increase. When comparing MgO and GnP suspensions, GnP samples reach higher thermal diffusivity values than MgO, with lower nanomaterials content. However, the dispersion of the results is higher in GnP suspensions.
- From rheological analysis, we found that MgO/PT8 suspensions are viscoplastic (behave as a solid at rest) whereas GnP/PT8 are viscoelastic (behave as a liquid at rest) with no presence of yield stress in the latter but in the former. This noticeable differentiated behaviour was thoroughly characterized, allowing us to assess the influence of the microscopic structural properties on the macroscopic mechanical behaviour. The size of MgO promotes the formation of large fractal agglomerates that forms a strong gel network within PT8 while the sheet-like shape of GnP favours the fluid-like behaviour of the nanofluids.

The findings here reported become essential to design optimized systems that use these novel engineered materials. We encourage researchers on nanofluids to accomplish comprehensively rheological investigations of their samples, avoiding the automatic use of viscometers without the determination of their flow behaviour, and, in the case of non-Newtonian behaviour, to perform tests to study the viscoelasticity of the nanofluids. By following this recommendation, we can better understand the behaviour of the nanofluids and assign them to specific applications accordingly, at the same time, have trustful literature data to compare with.

CRediT authorship contribution statement

Jose I. Prado: Conceptualization, Methodology, Investigation, Formal analysis, Writing – original draft, Writing – review & editing. **María Elena Navarro:** Conceptualization, Methodology, Investigation, Data curation, Writing – original draft, Writing – review & editing. **Uxía Calviño:** Investigation, Data curation, Writing – review & editing. **Yulong Ding:** Project administration, Validation, Supervision, Resources, Writing – review & editing. **Luis Lugo:** Project administration, Validation, Supervision, Resources, Writing – review & editing.

Declaration of Competing Interest

The authors declare that they have no known competing financial interests or personal relationships that could have appeared to influence the work reported in this paper.

Data availability

Data will be made available on request.

Acknowledgments

This work was supported by the "Ministerio de Economía y Competitividad" (Spain) and FEDER program through the ENE2017-86425-C2-1-R project. Grant PID2020-112846RB-C21 funded by MCIN/AEI/10.13039/501100011033. Grant PDC2021-121225-C21 funded by MCIN/AEI/10.13039/501100011033 and by "European Union NextGenerationEU/PRTR". The authors acknowledge the financial support by the Xunta de Galicia (Spain) through GRC ED431C 2020/06 Program. This work was also partially supported by COST Action CA15119: Overcoming Barriers to Nanofluids Market Uptake (Nanouptake) in the framework of the Short-Term Scientific Mission program. J.I.P. acknowledges the financial support by the Ministerio de Universidades (Spain) under budgetary implementation 33.50.460A.752 and by the European Union NextGenerationEU/PRTR through a Margarita Salas postdoctoral contract of the Universidade de Vigo (Spain). U.C. acknowledges the financial support from "Agencia Estatal de Investigación" under predoctoral grant PRE2021-097589. Funding for open access charge: Universidade de Vigo/CISUG.

References

[1] G. Coccia, S. Tomassetti, G. Di Nicola, Renew. Sust. Energ. Rev. 151 (2021), 111573.
[2] I.A. Popov, Y.F. Gortyshov, V.V. Olimpiev, Therm. Eng. 59 (2012) 1.
[3] M. Krishnam, S. Bose, C. Das, Appl. Therm. Eng. 106 (2016) 951.
[4] B. Jo, D. Banerjee, J. Heat Transfer 137 (2015).
[5] T. Bauer, N. Breidenbach, N. Pfleger, D. Laing, M. Eck, World Renewable Energy Forum, Denver, Colorado, US, 2012.
[6] R.B. Ganvir, P.V. Walke, V.M. Kriplani, Renew. Sust. Energ. Rev. 75 (2017) 451.
[7] J.P. Vallejo, J.I. Prado, L. Lugo, Appl. Therm. Eng. 203 (2022), 117926.
[8] Y.R. Sekhar, K.V. Sharma, J. Exp. Nanosci. 10 (2015) 86.
[9] B. Jo, D. Banerjee, Acta Materialia 75 (2014) 80.
[10] P. Kumar, D. Dey, S. Samantaray, 2016 International Conference on Electrical, Electronics, and Optimization Techniques (ICEEOT), 2016, p. 3555-3560.
[11] M. Mehrali, E. Sadeghinezhad, S.T. Latibari, S.N. Kazi, M. Mehrali, M.N.B.M. Zubir, H.S.C. Metselaar, Nanoscale Res. Lett. 9 (2014) 15.
[12] S.F. Ahmed, M. Khalid, N. Amin, W. Rashmi, J. Mater. Sci. 53 (2018) 692.
[13] S.M.S. Murshed, C.A. Nieto de Castro, Renew. Sust. Energ. Rev. 37 (2014) 155.
[14] B. Muñoz-Sánchez, J. Nieto-Maestre, E. Veca, R. Liberatore, S. Sau, H. Navarro, Y. Ding, N. Navarrete, J.E. Juliá, Á.G. Fernández, A. García-Romero, Sol. Energy Mater. Sol. Cells 176 (2018) 357.
[15] O. Mahian, A. Kianifar, A.Z. Sahin, S. Wongwises, Energ. Convers Manage. 88 (2014) 129.
[16] C. Wang, J. Yang, Y. Ding, Prog. Nat. Sci.: Mater. Int. 23 (2013) 338.
[17] N.K. Gupta, A.K. Tiwari, S.K. Ghosh, Exp. Therm. Fluid Sci. 90 (2018) 84.
[18] G. Żyła, J.P. Vallejo, J. Fal, L. Lugo, Int. J. Heat Mass Transf. 121 (2018) 1201.
[19] G. Żyła, J. Mol. Liq. 297 (2020), 111732.
[20] F. Wang, X. Fang, Z. Zhang, Sol. Energy Mater. Sol. Cells 176 (2018) 381.
[21] H. Liu, X. Wang, D. Wu, Sustainable Energy & Fuels 3 (2019) 1091.
[22] J.I. Prado, U. Calviño, L. Lugo, J. Mol. Liq. 360 (2022), 119456.
[23] T. Shi, M. Zhang, H. Liu, X. Wang, Sol. Energy Mater. Sol. Cells 248 (2022), 112016.
[24] J.I. Prado, L. Lugo, A.C.S. Appl, Mater. Interfaces 12 (2020) 39108.
[25] S. Manikandan, K.S. Rajan, Energy 88 (2015) 408.
[26] M. Pavía, K. Alajami, P. Estellé, A. Desforges, B. Vigolo, Adv. Colloid Interface Sci. 294 (2021), 102452.
[27] D. Cabaleiro, C. Gracia-Fernández, L. Lugo, J. Chem. Thermodyn. 74 (2014) 43.
[28] Q. Yi, S. Tan, C. Jiang, X. Guan, Y. Wu, Energy Build. 152 (2017) 442.
[29] R.I. Olivares, C. Chen, S. Wright, J. Sol. Energy Eng. 134 (2012).
[30] C. Vélez, M. Khayet, J.M. Ortiz de Zárate, Appl. Energy 143 (2015) 383.
[31] A. Palacios, L. Cong, M.E. Navarro, Y. Ding, C. Barreneche, Renew. Sust. Energ. Rev. 108 (2019) 32.
[32] M. Sandhya, D. Ramasamy, K. Sudhakar, K. Kadirgama, M. Samykano, W.S. W. Harun, G. Najafi, M. Mofijur, M. Mazlan, Sustainable Energy Technologies and Assessments 44 (2021), 101058.
[33] X. Wang, L. Guo, Colloids Surf. A: Physicochem. Eng. Asp. 304 (2007) 1.
[34] M. Hemmat Esfe, M. Mosaferi, J. Mol. Liq. 309 (2020), 112632.
[35] K. Yapici, O. Osturk, Y. Uludag, Braz. J. Chem. Eng. 35 (2018) 575.
[36] Ç. Demirkır, H. Ertürk, Int. J. Heat Mass Transf. 149 (2020), 119113.
[37] J.P. Vallejo, G. Żyła, J. Fernández-Seara, L. Lugo, Int. Commun. Heat Mass Transf. 99 (2018) 43.
[38] W.H. Herschel, R. Bulkley, Kolloid-Zeitschrift 39 (1926) 291.
[39] M.M. Cross, J. Colloid Sci. 20 (1965) 417.
[40] P. Estellé, G. Żyła, in: S.M.S. Murshed (Ed.) Fundamentals and Transport Properties of Nanofluids, The Royal Society of Chemistry, 2022.
[41] R.G. Larson, J. Rheol. 49 (2005) 1.
[42] P. Coussot, C. Ancey, Phys. Rev. E 59 (1999) 4445.
[43] C. Allain, M. Cloitre, M. Wafra, Phys. Rev. Lett. 74 (1995) 1478.
[44] D. Song, H. Jin, J. Jin, D. Jing, J. Phys. D 49 (2016), 425303.
[45] W.Y. Shih, W.-H. Shih, I.A. Aksay, J. Am. Ceram. Soc. 82 (1999) 616.
[46] F. Hausdorff, Math. Ann. 79 (1918) 157.
[47] S. Lazzari, L. Nicoud, B. Jaquet, M. Lattuada, M. Morbidelli, Adv. Colloid Interface Sci. 235 (2016) 1.
[48] M.Y. Lin, H.M. Lindsay, D.A. Weitz, R.C. Ball, R. Klein, P. Meakin, Nature 339 (1989) 360.
[49] J.D.F. Ramsay, S.R. Daish, C.J. Wright, Faraday Discuss. 65 (1978) 65.
[50] S. Aben, C. Holtze, T. Tadros, P. Schurtenberger, Langmuir 28 (2012) 7967.
[51] C. Gracia-Fernandez, S. Gómez-Barreiro, J. López-Beceiro, S. Naya, R. Artiaga, J. Therm. Anal. Calorim. 115 (2014) 1727.
[52] N.E. Marcovich, M.L. Auad, N.E. Bellesi, S.R. Nutt, M.I. Aranguren, J. Mater. Res. 21 (2006) 870.